AGU ADVANCING EARTH AND SPACE SCIENCES

JGR Space Physics

Global Distribution of Relativistic Electron Precipitation and the Dependences on Substorm Injection and Solar Wind Ram Pressure: Long-Term POES Observations

Huayue Chen[1,2] , Xinliang Gao[1,3] , Quanming Lu[1,3] , and Bruce T. Tsurutani[4]

[1]Deep Space Exploration Laboratory, School of Earth and Space Sciences, University of Science and Technology of China, Hefei, China, [2]Department of Physics, Auburn University, Auburn, AL, USA, [3]CAS Center for Excellence in Comparative Planetology, Hefei, China, [4]Retired, Pasadena, CA, USA

Abstract Relativistic electron precipitation (REP) into the Earth's atmosphere is one of the fundamental mechanisms causing radiation belt electron flux dropout. It is important to know the preferred regions of REP events and the interplanetary and magnetospheric conditions under which the events take place. In this study of the POES relativistic electron data during 1998–2017, we have examined all REP events from $L = 3$–10 using an automatic algorithm. The REP events preferentially occur in MLT = 17–03 at $L = 4$–6.5, where the precipitation fluxes also peak. The monthly average REP event number is correlated with both monthly average AE (auroral electrojet index) and P_d (solar wind ram pressure) indices, so we separately investigate the spatial dependences of the events on one index by restricting the other one to a low level. The occurrence rate of REP events increases with both the AE* and the P_d^* indices (where AE* and P_d^* are time-modified from the AE and P_d indices). During large AE* but low P_d^*, the events occur mainly in the dusk sector (MLT = 17–22) near the plasmapause. For large P_d^* but low AE* intervals, most of the events occur outside the plasmapause in the midnight sector (MLT = 23–03). Possible REP loss mechanisms are discussed based on our findings. Our study provides new insights into the distribution and dependences of REP in the Earth's magnetosphere.

1. Introduction

The Earth's radiation belt is a donut-shaped zone filled with relativistic (~MeV) electrons, whose flux can fluctuate by several orders of magnitude during disturbed periods (Hajra & Tsurutani, 2018; Reeves et al., 2003; Summers et al., 2007). Both geomagnetic activities and solar wind variations can cause significant relativistic electron flux changes in the radiation belt. For example, Hua et al. (2022) found that the relativistic electron flux depends on substorm injections, and is strongly correlated with the time-integral AL index. Wing et al. (2022) suggested that the solar wind ram pressure can modulate the electron flux at $L^* > 3.5$. The loss processes, as well as the acceleration processes, are believed to play a fundamental role in controlling the electron dynamics in the radiation belt (Bortnik et al., 2006; Gao et al., 2015; Hajra & Tsurutani, 2018; Horne & Thorne, 2003; Tsurutani et al., 2016). Relativistic electron precipitation (REP) into the Earth's atmosphere is an important loss mechanism, in which the electrons are scattered into the loss cones and are lost by collisions with neutral particles (Horne & Thorne, 2003; Summers et al., 2007; Tsurutani & Lakhina, 1997; Tsurutani et al., 2016). However, the specific mechanisms of electron scattering are still under debate.

Plasma waves have been widely considered to be responsible for the electron scattering (Horne & Thorne, 2003; Summers et al., 2007). Electromagnetic Ion Cyclotron (EMIC) waves are one of the most promising candidates (Carson et al., 2013; Miyoshi et al., 2008; Remya et al., 2015). This is a "parasitic interaction" where unstable ion distributions generate EMIC waves and the waves then pitch angle scatter the preexisting electrons. Theoretical results have shown that EMIC waves can resonantly scatter electrons with energies larger than ~1 MeV near the magnetic equator where the waves are coherent and the magnetic fields are weakest (Remya et al., 2015; Tsurutani et al., 2016). Simultaneous detections of EMIC waves and REP events have been reported (Miyoshi et al., 2008), providing observational support for this mechanism. Moreover, plasmaspheric hiss waves, which are preferentially detected inside the plasmasphere or in the high-density plumes external to the plasmasphere (Li et al., 2013; Meredith et al., 2018; Thorne et al., 1973; Tsurutani et al., 2015), can typically pitch angle scatter the relativistic electron on the dayside (Agapitov et al., 2020).

Chorus waves can also cause REP events via cyclotron resonance (Horne et al., 2005; Kang et al., 2022; Lakhina et al., 2010; Tsurutani et al., 2013). This mechanism would also be a "parasitic interaction," where the temperature anisotropic electrons in 10 s keV excite chorus waves and the waves in turn pitch angle scatter the preexisting relativistic electrons (Lakhina et al., 2010; Miyoshi et al., 2020). Such wave-particle interactions can take place only at high magnetic latitudes away from the magnetic equator (Horne & Thorne, 2003). Tsurutani et al. (2011) have shown that chorus becomes quasi-coherent and even incoherent as the waves propagate away from the magnetic equator. If the waves are incoherent where the waves are in cyclotron resonance with relativistic electrons, no REP will be produced (Tsurutani et al., 2011). The observations of precipitating relativistic electrons in auroral pulsating patches (Miyoshi et al., 2020; Shumko et al., 2021) is exciting news.

Besides plasma waves, highly curved magnetic field line is another potential candidate, often referred to as "field line curvature (FLC) scattering." This mechanism mainly occurs in the nightside magnetosphere, where field lines are stretched (small B_z, with B_z being the equatorial magnetic normal component; Ohtani & Motoba, 2017), thin current sheets are present (Sergeev et al., 1983, 2012), and the curvature radius of these lines becomes comparable to the electron's gyroradius (Imhof, 1988; Sergeev & Tsyganenko, 1982). The FLC scattering typically takes place poleward of the isotropic boundary (IB) (Sergeev et al., 1983, 2012), which is the boundary between isotropic (i.e., trapped fluxes equal precipitation fluxes) and anisotropic fluxes. The stretched field lines on the nightside can be reproduced in empirical models (e.g., Tsyganenko & Sitnov, 2007), and have been detected in situ (with a curvature radius of ∼0.05 Earth radius) by multi-point Cluster satellites (Zhang et al., 2016).

Many studies have been performed to investigate the global distribution of REP events. Bortnik et al. (2006) proposed that the REP events typically occur at small L-shells ($L < 5$). By using POES data with a resolution of 16-s, Shekhar et al. (2017) investigated the L-shell coverage (δL) of REP events. They found that the events in the early morning and dusk sectors are more localized in L-shell, with $\delta L < 0.5$. On the nightside, the events cover a wider L-shell with $\delta L = 1$–2.5. Gasque et al. (2021) modified the study of Shekhar et al. (2017) by using the POES data with a higher resolution (2-s), and indicated that the REP events typically cover a very small L-shell range ($\delta L < 0.2$).

Yahnin et al. (2016) investigated the potential drivers of REP events by analyzing the morphology of particle fluxes. They categorized REP events into three groups. In the first group, REP occurs just at the IB of relativistic electrons. Moreover, the IB of electrons with lower energies moves poleward, while that of ∼10 keV protons moves equatorward. These events are mainly on the nightside, and can be explained by the FLC scattering (Capannolo et al., 2022; Imhof, 1988; Sergeev & Tsyganenko, 1982; Smith et al., 2016). The events in the second group occur with the precipitation of lower energy electrons and are detected at almost all MLT regions, and are driven by plasmaspheric hiss waves or upper hybrid resonance (UHR) waves. The events in the third group occur with the precipitation fluxes of ∼10 keV protons, and are typically in the dusk sector, being considered to be caused by EMIC waves.

Carson et al. (2013) presented the global distribution of EMIC-driven REP events, defined by simultaneous precipitation of ∼1 MeV electrons and ∼10 keV protons, and showed that the high occurrence rates are at $L = 4$–7 both in the dusk and night sectors. However, Smith et al. (2016) proposed that some simultaneous precipitation of relativistic electrons and energetic protons may be caused by the FLC scattering, which is mistaken for EMIC wave scattering. Since the IB of ∼10 keV protons is more equatorward than that of the relativistic electrons, ∼10 keV protons are also precipitated by highly curved field when REP occurs. Capannolo et al. (2022) further supported this idea by showing the coexistence of REP events scattered by EMIC waves and highly curved field lines. With 8-year of POES data, they found that there is no significant difference between the preferred regions of two kinds of events on the nightside, both with high occurrence rates at $L = 4$–7. Moreover, when either kind of event occurs, the magnetic field becomes more curved than usual. Therefore, the two mechanisms may not be distinguished just from positions of where REP events are detected.

The distribution of REP events has been systematically investigated by previous studies (Capannollo et al., 2022; Carson et al., 2013; Gasque et al., 2021; Shekhar et al., 2017; Yahnin et al., 2016). Nevertheless, the spatial dependences of REP events on geomagnetic activity and solar wind variations have not been fully understood, which plays an important role in determining the drivers of REP events. In this study, we first identify REP events during nearly two solar cycles (1998–2017) by using POES satellites data. Then separately investigate the dependences of REP events on substorm injections and solar wind ram pressure. The relative distances between REP events and the plasmapause have been further studied.

2. Data and Instruments

The particle's fluxes are selected from five NOAA-POES (NOAA15-NOAA19) and two MetOp (MetOp-01 and MetOp-02) satellites, which operate in Sun-synchronous polar orbits at an altitude of ∼800 km. The onboard Medium Energy Proton and Electron Detector (MEPED) instrument has two solid-state telescopes (∼0° telescope and ∼90° telescope, each with a pitch angle width of ∼±15°) to measure the electron and proton fluxes with a time resolution of 2 s (Evans & Greer, 2004), where the ∼0° telescope can detect the precipitating fluxes (marked as J_0) inside the loss cone at $L > 2$ (Rodger et al., 2010). The electron telescopes contain three energy channels (E1-E3), while the proton telescopes have six channels (P1-P6). The P6 channel is designed to measure the proton fluxes with $E_k > 6.9$ MeV, but it is severely contaminated by the relativistic electrons with $E_k > 0.8$ MeV (Miyoshi et al., 2008). The P5 channel (monitoring the proton fluxes with $E_k = 2.5–6.9$ MeV) is not contaminated (Yando et al., 2011). Therefore, the P6 channel can be used to monitor the relativistic electron fluxes when there is no response in the P5 channel.

The solar wind ram pressure (P_d) and geomagnetic indices (AE and SymH) with 1-min time resolution are obtained from the OMNI website (https://omniweb.gsfc.nasa.gov), where the P_d is time-shifted to the Earth's bow shock nose. The data of monthly average sunspot numbers are obtained from the SILSO website (http://www.sidc.be/silso/home).

3. Observational Results

3.1. Identification Algorithm

To analyze a large amount of data from seven POES satellites, we utilize an algorithm to identify the REP events automatically. Here, the measurements in P5 and P6 channels of the ∼0° telescope are used. The identification procedure is listed below:

1. Using a geometric factor $G \sim 0.01$ cm^2 sr (Yando et al., 2011), the particle's flux J_0 is estimated from the number count per second C by $J_0 = C/G$.
2. Perform a running average of 30-s (15 data points) to the J_0 data of the P6 channel. Any measured flux that exceeds the running average by a factor of 3 or more is taken as a potential REP event (A factor of 2.5 is also tested, with essentially the same results). To remove the spikes or other noise, the measurements at the previous and the following time points are required to be greater than 100 cm^{-2} s^{-1} sr^{-1}, and the running average at this time point is greater than 150 cm^{-2} s^{-1} sr^{-1}.
3. The P5 channel has no response within the time interval of 5-min before and after the selected time point, ensuring that the responses in the P6 channel are only due to relativistic electrons.
4. Any events occurring within the South Atlantic Anomaly region (spanning from −52° to 20° geographic latitude and from −180° to 30° longitude; Rodger et al., 2010), or during the period of solar proton events (using the timetable from the NOAA Space Environment Center, https://umbra.nascom.nasa.gov/SEP) are excluded from further analysis to avoid contamination.

Two typical REP events (marked by red crosses) at 12:12:36 UT and 12:12:50 UT on 19 March 2015 detected by the NOAA-15 satellite are shown in Figure 1a, where the blue line represents the J_0 data of the P6 channel, and the black line denotes the 30-s average values of J_0. At 12:12:36 UT, the measured flux (5,600 cm^{-2} s^{-1} sr^{-1}) is 3.4 times larger than the average value (1,660 cm^{-2} s^{-1} sr^{-1}), and the ratio is 3.3 at 12:12:50 UT (with the measured flux of 5,300 cm^{-2} s^{-1} sr^{-1} and the average value of 1,590 cm^{-2} s^{-1} sr^{-1}). During 12:06:00–12:18:00 UT, the P5 channel has no response at all (not shown), indicating that the detected P6 channel signal only corresponds to the relativistic electrons.

3.2. Statistical Results

During the interval from 1998 to 2017, 90,970 REP events were identified in the range of $L = 3–10$ using the algorithm described above. Figure 1 shows the global distributions of (b) the total dwell time of seven POES satellites, (c) the occurrence rate and (d) the median flux of REP events in the L-MLT planes. The magenta circles mark the geosynchronous orbits (i.e., $L = 6.6$). Although each POES satellite is designed to orbit at two preferred MLT regions, several satellites have experienced significant drift in MLT (Sandanger et al., 2015). Therefore, their MLT coverage is almost uniform except for the reduced coverage around MLT = 12 (Figure 1b). Even so,
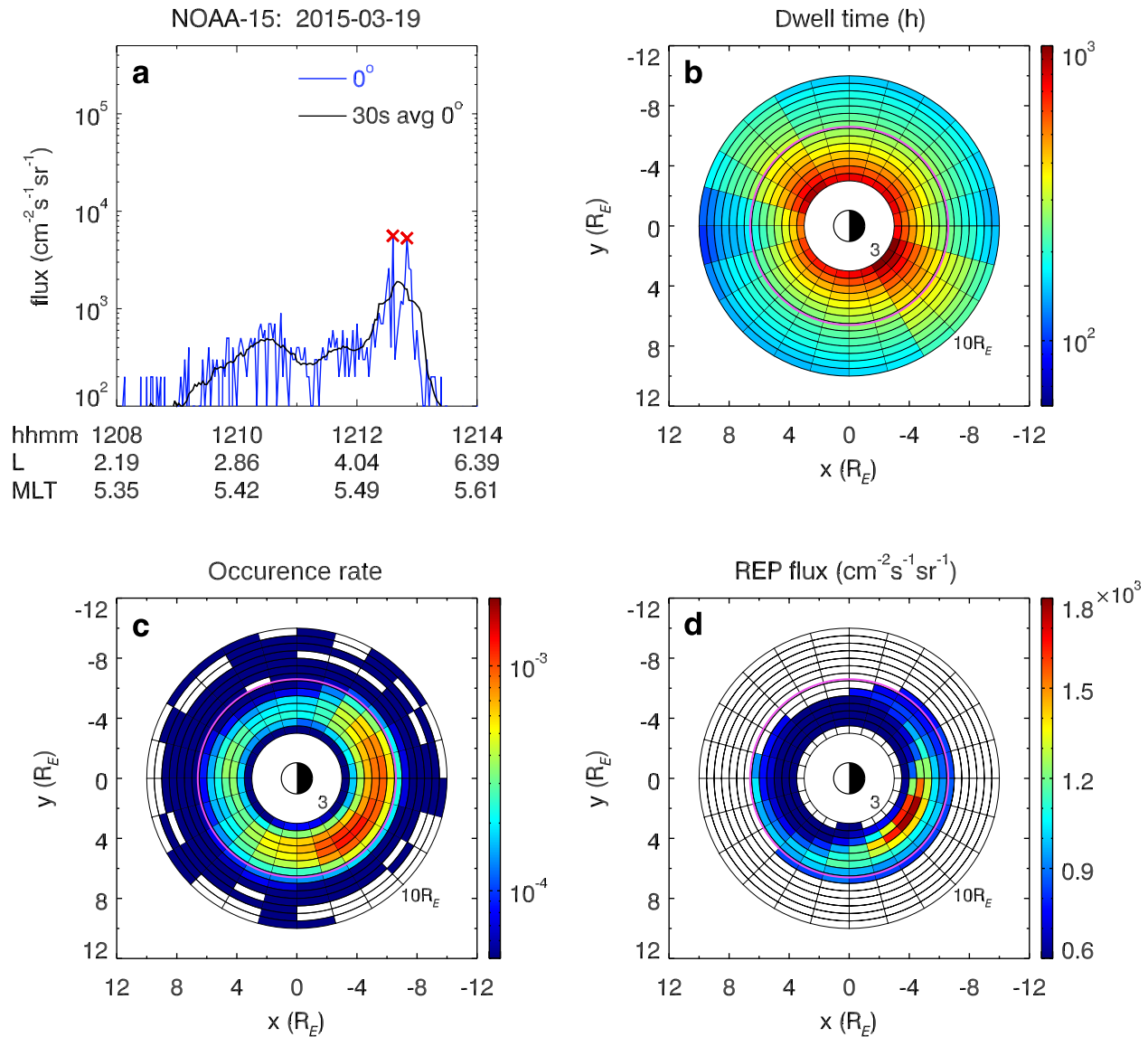
Figure 1. (a) The electron fluxes in the P6 channel, which are measured by NOAA-15 on 19 March 2015. The blue line denotes the precipitation fluxes, and the black line represents their 30-s average values. The two REP events have been marked by red crosses at 12:12:36 UT and 12:12:50 UT, respectively. The global distributions of (b) the total dwell time of seven POES satellites, (c) the occurrence rate of REP events, and (d) the median values of REP fluxes in the L-MLT planes, where the magenta circle in each panel represent the geosynchronous orbit at $L = 6.6$.

the bin with the minimum dwell time still has at least 70 hr (126,000 time points), ensuring that the results are statistically significant. According to the distribution of occurrence rate (Figure 1c), which is defined as the ratio between the total detection time of REP events and the total dwell time of satellites in each bin, the REP events preferentially occur in the dusk and midnight (MLT = 17–03) sectors at $L = 4$–6.5, with an occurrence rate of $\sim 10^{-3}$. While, outside the geosynchronous orbit, their occurrence rates are quite low ($\sim 10^{-4}$). The fluxes of REP events are further investigated (Figure 1d), where the median value of the REP fluxes in each bin is shown. To reduce statistical error, the bins with occurrence rates lower than 10^{-4} are discarded. The fluxes of REP events remain nearly constant ($\sim 0.8 \times 10^{-3}$ cm^{-2} s^{-1} sr^{-1}), except in the pre-midnight (MLT = 20–00) sector at $L = 4$–5.5, where the fluxes are somewhat higher ($\sim 1.7 \times 10^{-3}$ cm^{-2} s^{-1} sr^{-1}).

Figure 2 shows the monthly average values of (a) the number of REP events, (b) the AE index, (c) the SymH index, (d) the solar wind ram pressure P_d, and (e) the sunspot number. The correlation coefficients ρ between the number of REP events and each index is calculated, where the strongest correlation corresponds to $|\rho| = 1$, and $\rho = 0$ denotes no correlation. Among all the indices, the number of REP events is highly dependent on the AE
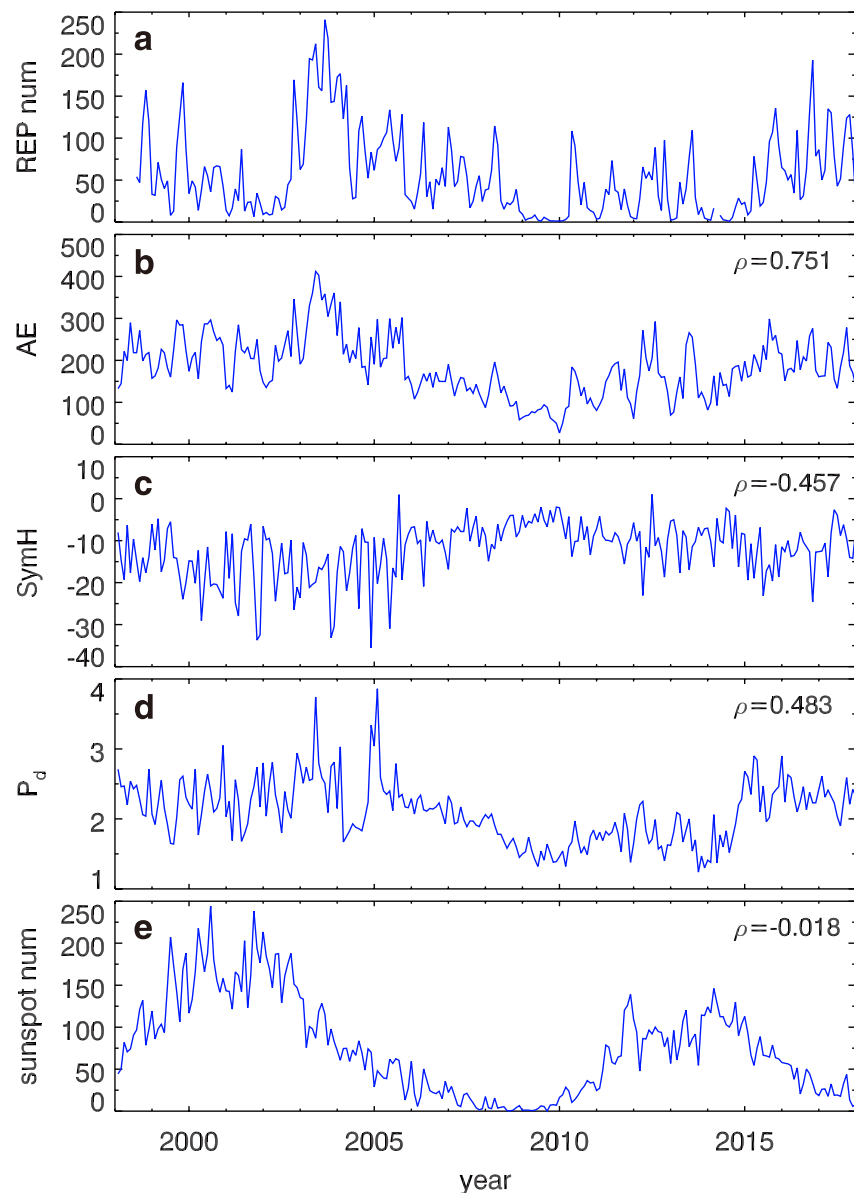
Figure 2. The monthly average values of (a) the number of REP events, (b) the AE index, (c) the SymH index, (d) solar wind ram pressure P_d, and (e) sunspot number. In panels (b–e), the correlation coefficients between the number of REP events and each index are displayed.

index with $\rho = 0.751$, while the correlations with SymH and P_d indices are relatively weaker but still significant (with $\rho = -0.457$ and 0.483, respectively). The correlation with the sunspot number seems to be quite weak with $\rho = -0.018$. It is interesting to find that the REP events are preferentially detected during the declining phase of the solar cycle (2003–2009 and 2015–2018), while they are not significantly observed during 2009–2010 and 2014–2015, corresponding to the solar minimum and the solar maximum, respectively.

During substorms (large AE), the energetic particles are injected into the magnetosphere and are unstable to excite plasma waves (e.g., EMIC waves and plasmaspheric hiss waves) (Ma et al., 2022; Tsurutani et al., 2015). When the solar wind pressure (P_d) is enhanced, the dayside magnetosphere is compressed, which is also suitable for wave excitation (Chen et al., 2020; Olson & Lee, 1983; Tsurutani et al., 2016). Therefore, both AE and P_d indices play an important role in exciting waves, which are responsible for electron scattering and resulting precipitation. We further investigate the dependences of REP events on the two indices. Since there is a time delay between REP detection and AE or P_d index caused by different locations of data measurement, we perform
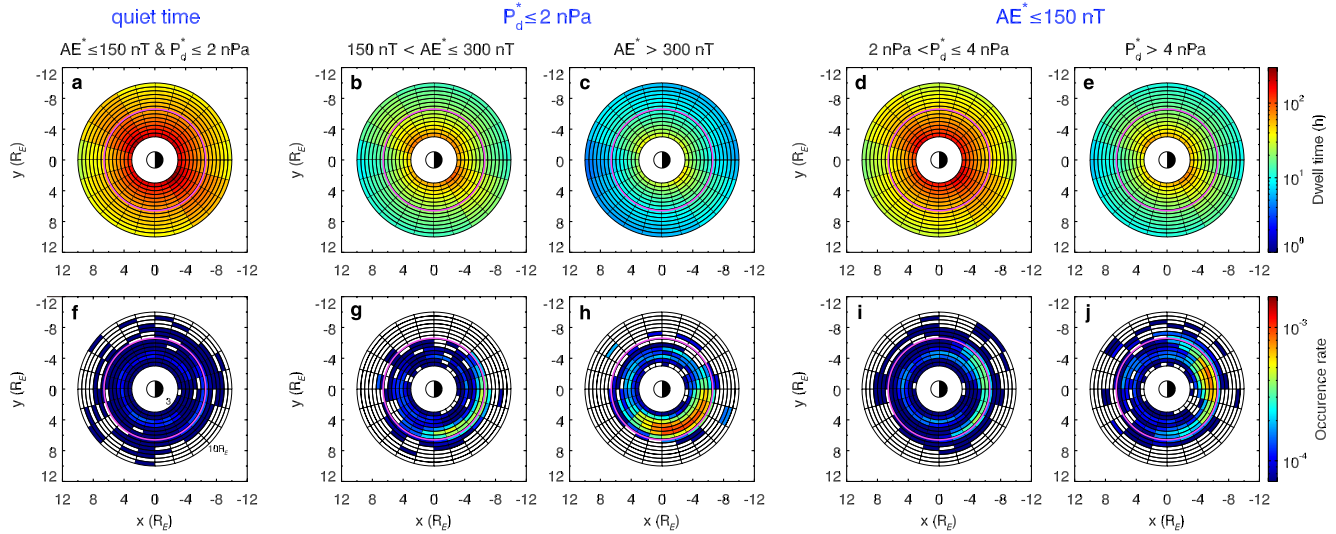
Figure 3. The distribution of (a–e) the dwell time of satellites, and (f–j) the occurrence rate of REP events in the L-MLT planes. The columns from left to right correspond to the periods of (a, f) quiet time ($AE^* \leq 150$ nT and $P_d^* \leq 2$ nPa), (b, g) low P_d^* ($P_d^* \leq 2$ nPa) but moderate AE^* (150 nT $< AE^* \leq 300$ nT), (c, h) low P_d^* ($P_d^* \leq 2$ nPa) but strong AE^* ($AE^* > 300$ nT), (d, i) weak injection ($AE^* \leq 150$ nT) but moderate P_d^* (2 nPa $< P_d^* \leq 4$ nPa), (e, j) weak injection ($AE^* \leq 150$ nT) but strong P_d^* ($P_d^* > 4$ nPa). The magenta circles represent the geosynchronous orbits.

a time modification to the two indices (i.e., AE^* and P_d^*). REP events can be produced by EMIC waves excited by energetic protons during substorms (Carson et al., 2013; Miyoshi et al., 2008), so the AE index is modified by considering the drift time of protons. The protons are assumed to be injected in the range of MLT = 21–01 (Lopez et al., 1990), with the drift velocity given by

$$\overrightarrow{V_{\mathrm{dri}}} = \frac{\mu}{e\gamma} \frac{\vec{b} \times \nabla B}{B} + \frac{p_\parallel^2}{e\gamma m_p} \frac{\vec{b} \times (\vec{b} \cdot \nabla)\vec{b}}{B} \tag{1}$$

where $\vec{b}$ is the unit of the magnetic field, e and m_p are the charge and mass of the proton, and μ, γ, and $p_\parallel$ are the magnetic momentum, relativistic factor, and parallel momentum, respectively. At time T_0, the satellite is located at MLT_0 and L_0. For simplicity, the dipole magnetic model is used, and the equatorial pitch angle and the kinetic energy of the proton are set as $\alpha_{\mathrm{eq}} = 45°$ and $E_k = 25$ keV (Chen et al., 2019). The drift time in a complete drift path is $T_D = 2\pi r_0 / V_{\mathrm{dri}}$ (with $r_0 = L_0 R_E$). Generally, the longest drift time is defined as the drift time from MLT = 01 to MLT_0 with $T_L = T_D \times (24 - MLT_0 + 1)/24$, while the shortest drift time is the drift time from MLT = 21 to MLT_0 with $T_S = T_D \times (24 - MLT_0 - 3)/24$. The AE^* index is defined as the largest AE value in the time interval from $T_0 - T_L$ to $T_0 - T_S$. However, if MLT_0 is just in the range of 21–01, the AE^* represents the largest AE value in the interval from $T_0 - T_D$ to T_0. The details can be referred to in Chen et al. (2020). The P_d^* index is defined as the maximum value in the previous 10 min, because it only takes several minutes for the solar wind to move from the bow shock nose to $L \sim 6$ (Ma et al., 2022). In our study, the dependence of REP events on each index is investigated alone, by simultaneously restricting the other index to a low level. These events are classified into five categories: low P_d^* and low AE^* ($P_d^* \leq 2$ nPa and $AE^* \leq 150$ nT), low P_d^* ($P_d^* \leq 2$ nPa) but moderate AE^* (150 nT $< AE^* \leq 300$ nT), low P_d^* ($P_d^* \leq 2$ nPa) but strong AE^* ($AE^* > 300$ nT), low AE^* ($AE^* \leq 150$ nT) but moderate P_d^* (2 nPa $< P_d^* \leq 4$ nPa), and low AE^* ($AE^* \leq 150$ nT) but strong P_d^* ($P_d^* > 4$ nPa). Accordingly, there are 2378, 1231, 798, 2663, and 1339 REP events in each category, respectively.

Figure 3 illustrates (a-e) the total dwell time of POES satellites, and (f-j) the occurrence rate of REP events in the L-MLT planes (with a bin size of 0.5 L × 1 MLT). The occurrence rate is defined as the ratio between the total detection time of REP events and the total dwell time of satellites in the same bin and the same category. As shown in Figures 3a–3e, the coverage of satellites is nearly uniform over all MLTs except the noon (MLT = 12) and midnight (MLT = 00) sectors. During quiet periods (Figure 3f), the occurrence rates of REP events are quite low, but are slightly higher in over MLT = 01–21 at $L = 4$–5 and in over MLT = 20–03 at $L = 6$–7. As AE^* increases while P_d^* remains low (Figures 3g and 3h), REP events are preferentially detected in the dusk sector
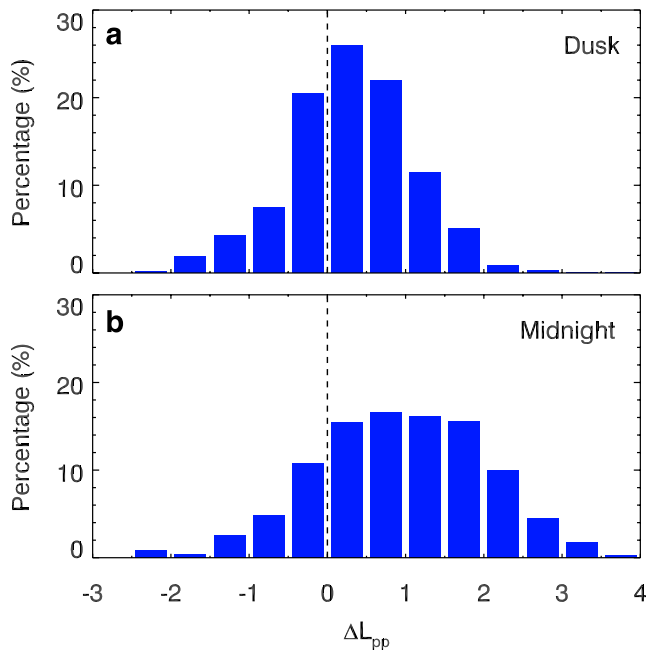
Figure 4. The percentage of REP events as a function of ΔL_{pp} in the (a) dusk sector (MLT = 17–22) and (b) midnight sector (MLT = 23–03), where ΔL_{pp} represents the distance between a REP event and plasmapause. The dashed lines at $\Delta L_{pp} = 0$ mark the position of the plasmapause.

(MLT = 17–22) at $L > 5$ with an occurrence rate of $\sim 1 \times 10^{-3}$, which is consistent with the drift path of substorm-injected protons. However, under the conditions of low AE* but moderate or high P_d^* (Figures 3i and 3j), the occurrence rates of REP events are significantly enhanced ($\sim 8 \times 10^{-4}$) in the midnight sector (MLT = 23–03) at $L > 5$. The events also have subtle higher occurrence rates ($\sim 3 \times 10^{-4}$) at $L = 4$–5 over all MLTs except the pre-midnight sector. Moreover, the occurrence rate of REP events increases with both the AE* index and the P_d^* index. The different favored regions of REP events suggest that they probably have different drivers.

There are 1585 and 2741 REP events in the dusk (MLT = 17–22) and midnight (MLT = 23–03) sectors at $L > 4$. Since the plasmapause has a significant influence on plasma waves (e.g., EMIC waves and plasmaspheric hiss waves), we further investigate the distribution of REP events relative to the plasmapause (L_{pp}) in the two favored regions. Here, the L_{pp} at different MLT is estimated according to the model in O'Brien and Moldwin (2003), and ΔL_{pp} represents the distance between a REP event and the L_{pp}, with a positive (negative) ΔL_{pp} value representing outside (inside) the plasmapause. Figure 4 displays the percentage of REP events as a function of ΔL_{pp} in the (a) dusk and (b) midnight sectors, where the dashed lines mark the position of plasmapause. As shown in Figure 4a, the percentage of REP events in the dusk sector peaks quite close to the plasmapause, with 34.3% of the events inside it and 65.7% outside it. While the REP events in the midnight sector are mainly (80.6%) detected outside the plasmapause, with the percentage peaking at $\sim 1 R_E$ away from the plasmapause. Therefore, the relative distances to the plasmapause are different between the events in the two sectors.

4. Conclusions and Discussion

Using POES satellites data over nearly two solar cycles (1998–2017), we have statistically studied the distribution of REP events. The events are generally detected over MLT = 17–03 at $L = 4$–6.5, where the intensities are also the highest. The spatial dependences of REP events on the AE* and P_d^* indices have been separately investigated. During the periods of low P_d^* but large AE*, the REP events are mainly in the dusk sector (MLT = 17–22) near the plasmapause. While under the conditions of low AE* but large P_d^*, the events are preferentially in the midnight sector (MLT = 23–03), and are mainly $\sim 1 R_E$ outside the plasmapause. The occurrence rate of REP events increases with both the AE* index and the P_d^* index. Our study demonstrates the favored regions of REP events under different conditions in the Earth's magnetosphere.

The various preferred regions of REP events and their distinct distances to the plasmapause suggest that the events may have different drivers. The EMIC waves are one of the dominant drivers and are preferentially observed in the dusk sector (Chen et al., 2019, 2020). In our study, we find that the REP events are mainly detected in the dusk sector during large AE* (Figures 3g and 3h), which could be driven by substorm related EMIC waves. Carson et al. (2013) defined EMIC-driven REP events via the simultaneous precipitation of ~ 1 MeV electrons and ~ 10 keV protons, and found these events are preferentially located in the midnight sector. The REP events near the plasmapause in the midnight sectors have been observed in our study (Figures 3i, 3j, and 4b), which could also be caused by EMIC waves. However, more (80.6%) events are observed outside the plasmapause (with a distance of more than $1 R_E$) in the midnight sector (Figure 4b). These events can be driven by the FLC scattering when the curvature radius of field line is comparable with the gyroradius of $\sim$MeV electrons (Sergeev & Tsyganenko, 1982; Smith et al., 2016). Recently, Capannolo et al. (2022) try to distinguish the two mechanisms on the nightside, by proposing that the spatial isolated REP events (i.e., no precipitation before/after the REP events) are driven by EMIC waves, while the events exhibiting the energy dependence (where the electrons with lower energies are precipitated at outer L-shells) are caused by FLC scattering. However, they found that the two kinds of events coexist on the nightside, and may not be easily distinguished just from positions. To identify the dominant driver on the nightside, performing test particle simulation in various magnetic field topologies, such as those involving wave fields or exhibiting high curvature, is necessary. The simulation can enable us to

calculate the pitch angle diffusion coefficient for each of the two mechanisms. We leave it to a future study. The FLC scattering may also takes effect in the dust sector during large AE* periods. In these periods, the substorm-injected ions drift westward and the partial ring currents are enhanced (Donovan et al., 2003; Lvova et al., 2005; Tsyganenko & Sitnov, 2007). Then the magnetic field is more stretched in the dusk sector than in the dawn sector (Newell et al., 1998), promoting the FLC scattering.

Besides the above two mechanisms, REP can also be produced by plasmaspheric hiss waves (Agapitov et al., 2020), which are basically inside the plasmapause or in the high-density plumes (Meredith et al., 2018; Thorne et al., 1973; Tsurutani et al., 2015). In our study, REP events have subtly higher occurrence rates at $L < 5$, even during quiet periods (Figure 3f), which could be driven by plasmaspheric hiss waves.

We further find that the correlation coefficient between the monthly average REP event numbers and the monthly average P_d is moderate, which could potentially be attributed to two factors. On one hand, the enhanced solar wind pressure can not only induce wave excitation, but also contribute to electron loss by causing magnetopause shadowing (Bortnik et al., 2006; Gao et al., 2015; West et al., 1972). On the other hand, the intensity of REP events is related to both the pitch angle scattering rate and the relativistic electron fluxes in the radiation belt. The events have higher occurrence rates during the solar cycle declining phases (2003–2009 and 2015–2018). In these phases, the substorm injections are quite strong, providing more free energy for the excitation of chorus waves (Hajra & Tsurutani, 2018). Therefore, more relativistic electrons are accelerated due to chorus waves (Horne & Thorne, 2003; Horne et al., 2005; Hua et al., 2022), and precipitation become more pronounced consequently. Another possible factor is that during substorm injection, EMIC waves are also generated locally (Chen et al., 2020). Then anomalous cyclotron resonance between EMIC waves and the preexisting relativistic electrons can cause REP events (Tsurutani et al., 2016).

The REP events are rarely observed outside the geosynchronous orbit, which has three possible reasons. First, the trapped electron fluxes may be originally low here. Second, the electron losses at larger L-shells might primarily escape through the magnetopause shadowing (Bortnik et al., 2006; Gao et al., 2015; West et al., 1972). Lastly, the plasma conditions outside the geosynchronous orbit might not be favorable for EMIC waves to drive REP (Summers et al., 2007).

The intensity of electron fluxes in the radiation belt strongly depends on the preceding activity. Hua et al. (2022) found that the time delay between the relativistic electron fluxes and the time-integral AL index is around 10 days. Wing et al. (2022) suggested that the delay between relativistic electron fluxes and the plasma density n_{sw} (or velocity V_{sw}) of solar wind is around 10 hr. Moreover, substorm injection and solar wind pressure can also regulate the fluxes of sub-MeV electrons (Salice et al., 2023; Tyssoy et al., 2021). In this study, we use the time delay between the wave detection and the index measurement to modify the AE and P_d indices. Generally, the time delay of the P_d index is several minutes (Ma et al., 2022), and that of the AE index is several hours (Chen et al., 2020).

The large solar wind pressure can not only cause wave excitation on the dayside due to the compression of magnetic fields, but also change the topology of the magnetic field on the nightside (Axford, 1964; Song et al., 1999). Axford (1964) suggested that solar wind can drag the field lines on the nightside toward further distances via viscous force. Song et al. (1999) further supported this idea by showing a longer magnetotail is associated with a higher solar wind density or a faster solar wind velocity, which all correspond to a larger solar wind pressure. Therefore, during periods of large P_d^*, the magnetic fields on the nightside become more stretched highly curved, which is in favor of the FLC scattering. Moreover, Lvova et al. (2005) found that the IB of 80 keV protons shifts earthward during the period of large solar wind pressure, providing indirect evidence that the FLC scattering would take effect at relatively smaller L-shells ($L \sim 6$). The interplanetary shocks not only cause the compression of the dayside magnetosphere, but also trigger midnight sector substorm onsets within minutes of their arrival at the dayside magnetopause (Heppner, 1955; Zhou & Tsurutani, 2001). This type of events will be high solar wind pressure and low AE events. The delay in the substorm development in AE will preclude these events from this study.

Data Availability Statement

All the data from POES satellites are obtained online (https://www.ngdc.noaa.gov/stp/satellite/poes/dataaccess.html). The AE, SymH, and solar wind ram pressure data are from the OMNI website (https://omniweb.gsfc.nasa.gov), and the sunspot number data are obtained from the SILSO website (http://www.sidc.be/silso/home).

References

Agapitov, O., Mourenas, D., Artemyev, A., Claudepierre, S. G., Hospodarsky, G., & Bonnell, J. W. (2020). Lifetimes of relativistic electrons as determined from plasmaspheric hiss scattering rates statistics: Effects of ω_{pe}/Ω_{ce} and wave frequency dependence on geomagnetic activity. *Geophysical Research Letters*, *47*(13), e2020GL088052. https://doi.org/10.1029/2020GL088052

Axford, W. (1964). Viscous interaction between the solar wind and the Earth's magnetosphere. *Planetary and Space Science*, *12*(1), 45–53. https://doi.org/10.1016/0032-0633(64)90067-4

Bortnik, J., Thorne, R. M., O'Brien, T. P., Green, J. C., Strangeway, R. J., Shprits, Y. Y., & Baker, D. N. (2006). Observation of two distinct, rapid loss mechanisms during the 20 November 2003 radiation belt dropout event. *Journal of Geophysical Research*, *111*(A12), A12216. https://doi.org/10.1029/2006JA011802

Capannolo, L., Li, W., Millan, R., Smith, D., Sivadas, N., Sample, J., & Shekhar, S. (2022). Relativistic electron precipitation near midnight: Drivers, distribution, and properties. *Journal of Geophysical Research: Space Physics*, *127*(1), e2021JA030111. https://doi.org/10.1029/2021JA030111

Carson, B. R., Rodger, C. J., & Clilverd, M. A. (2013). POES satellite observations of EMIC-wave driven relativistic electron precipitation during 1998–2010. *Journal of Geophysical Research: Space Physics*, *118*(1), 232–243. https://doi.org/10.1029/2012JA017998

Chen, H., Gao, X., Lu, Q., Tsurutani, B. T., & Wang, S. (2020). Statistical evidence for EMIC wave excitation driven by substorm injection and enhanced solar wind pressure in the Earth's magnetosphere: Two different EMIC wave sources. *Geophysical Research Letters*, *47*(21), e2020GL090275. https://doi.org/10.1029/2020GL090275

Chen, H., Gao, X., Lu, Q., & Wang, S. (2019). Analyzing EMIC waves in the inner magnetosphere using long-term Van Allen Probes observations. *Journal of Geophysical Research: Space Physics*, *124*(9), 7402–7412. https://doi.org/10.1029/2019JA026965

Donovan, E. F., Jackel, B. J., Voronkov, I., Sotirelis, T., Creutzberg, F., & Nicholson, N. A. (2003). Ground-based optical determination of the b2i boundary: A basis for an optical MT-index. *Journal of Geophysical Research*, *108*(A3), 1115. https://doi.org/10.1029/2001JA009198

Evans, D. S., & Greer, M. S. (2004). *Polar orbiting environmental satellite space environment monitor-2: Instrument descriptions and archive data documentation*. NOAA technical Memorandum 93, version 1.4. Space Weather Prediction Center.

Gao, X., Li, W., Bortnik, J., Thorne, R. M., Lu, Q., Ma, Q., et al. (2015). The effect of different solar wind parameters upon significant relativistic electron flux dropouts in the magnetosphere. *Journal of Geophysical Research: Space Physics*, *120*(6), 4324–4337. https://doi.org/10.1002/2015JA021182

Gasque, L. C., Millan, R. M., & Shekhar, S. (2021). Statistically determining the spatial extent of relativistic electron precipitation events using 2-s polar-orbiting satellite data. *Journal of Geophysical Research: Space Physics*, *126*(4), e2020JA028675. https://doi.org/10.1029/2020JA028675

Hajra, R., & Tsurutani, B. T. (2018). Magnetospheric "killer" relativistic electron dropouts (REDs) and repopulation: A cyclical process. In *Extreme events in geospace* (pp. 373–399). Elsevier Inc. Chapter 14. https://doi.org/10.1016/B978-0-12-812700-1.00014-5

Heppner, J. P. (1955). Note on the occurrence of world-wide S.S.C's during onset of negative bays at College, Alaska. *Journal of Geophysical Research*, *60*(1), 29–32. https://doi.org/10.1029/jz060i001p00029

Horne, R. B., & Thorne, R. M. (2003). Relativistic electron acceleration and precipitation during resonant interactions with whistler-mode chorus. *Geophysical Research Letters*, *30*(10), 1527. https://doi.org/10.1029/2003GL016973

Horne, R. B., Thorne, R. M., Shprits, Y. Y., Meridith, N. P., Glauert, S. A., Smith, A. J., et al. (2005). Wave acceleration of electrons in the Van Allen radiation belts. *Nature*, *437*(8), 227–230. https://doi.org/10.1038/nature03939

Hua, M., Bortnik, J., Chu, X., Aryan, H., & Ma, Q. (2022). Unraveling the critical geomagnetic conditions controlling the upper limit of electron fluxes in the Earth's outer radiation belt. *Geophysical Research Letters*, *49*(22), e2022GL101096. https://doi.org/10.1029/2022GL101096

Imhof, W. L. (1988). Fine resolution measurements of the L-dependent energy threshold for isotropy at the trapping boundary. *Journal of Geophysical Research*, *93*(A9), 9743–9752. https://doi.org/10.1029/ja093ia09p09743

Kang, N., Bortnik, J., Zhang, X., Claudepierre, S., & Shi, X. (2022). Relativistic microburst scale size induced by a single point-source chorus element. *Geophysical Research Letters*, *49*(23), e2022GL100841. https://doi.org/10.1029/2022GL100841

Lakhina, G. S., Tsurutani, B. T., Verkhoglyadova, O. P., & Pickett, J. S. (2010). Pitch angle transport of electrons due to cyclotron interactions with coherent chorus subelements. *Journal of Geophysical Research*, *115*(A8), A00F15. https://doi.org/10.1029/2009JA014885

Li, W., Thorne, R. M., Bortnik, J., Reeves, G. D., Kletzing, C. A., Kurth, W. S., et al. (2013). An unusual enhancement of low-frequency plasmaspheric hiss in the outer plasmasphere associated with substorm-injected electrons. *Geophysical Research Letters*, *40*(15), 3798–3803. https://doi.org/10.1002/grl.50787

Lopez, R. E., Sibeck, D. G., McEntire, R. W., & Krimigis, S. M. (1990). The energetic ion substorm injection boundary. *Journal of Geophysical Research*, *95*(A1), 109–117. https://doi.org/10.1029/ja095ia01p00109

Lvova, E. A., Sergeev, V. A., & Bagautdinova, G. R. (2005). Statistical study of the proton isotropy boundary. *Annales Geophysicae*, *23*(4), 1311–1316. https://doi.org/10.5194/angeo-23-1311-2005

Ma, J., Gao, X., Chen, H., Tsurutani, B. T., Ke, Y., Chen, R., & Lu, Q. (2022). The effects of substorm injection of energetic electrons and enhanced solar wind ram pressure on whistler-mode chorus waves: A statistical study. *Journal of Geophysical Research: Space Physics*, *127*(11), e2022JA030502. https://doi.org/10.1029/2022JA030502

Meredith, N. P., Horne, R. B., Kersten, T., Li, W., Bortnik, J., Sicard, A., & Yearby, K. H. (2018). Global model of plasmaspheric hiss from multiple satellite observations. *Journal of Geophysical Research: Space Physics*, *123*(6), 4526–4541. https://doi.org/10.1029/2018JA025226

Miyoshi, Y., Saito, S., Kurita, S., Asamura, K., Hosokawa, K., Sakanoi, T., et al. (2020). Relativistic electron microbursts as high-energy tail of pulsating auroral electrons. *Geophysical Research Letters*, *47*(21), e2020GL090360. https://doi.org/10.1029/2020GL090360

Miyoshi, Y., Sakaguchi, K., Shiokawa, K., Evans, D., Albert, J., Connors, M., & Jordanova, V. (2008). Precipitation of radiation belt electrons by EMIC waves, observed from ground and space. *Geophysical Research Letters*, *35*(23), L23101. https://doi.org/10.1029/2008GL035727

Newell, P. T., Sergeev, V. A., Bikkuzina, G. R., & Wing, S. (1998). Characterizing the state of the magnetosphere: Testing the ion precipitation maxima latitude (b2i) and the ion isotropy boundary. *Journal of Geophysical Research*, *103*(A3), 4739–4745. https://doi.org/10.1029/97ja03622

O'Brien, T. P., & Moldwin, M. B. (2003). Empirical plasmapause models from magnetic indices. *Geophysical Research Letters*, *30*(4), 1152. https://doi.org/10.1029/2002GL016007

Ohtani, S., & Motoba, T. (2017). Equatorial magnetic field of the near-Earth magnetotail. *Journal of Geophysical Research: Space Physics*, *122*(8), 8462–8478. https://doi.org/10.1002/2017JA024115

Olson, J. V., & Lee, L. C. (1983). Pc1 wave generation by sudden impulses. *Planetary and Space Science*, *31*(3), 295–302. https://doi.org/10.1016/0032-0633(83)90079-X

Reeves, G. D., McAdams, K. L., Friedel, R. H. W., & O'Brien, T. P. (2003). Acceleration and loss of relativistic electrons during geomagnetic storms. *Geophysical Research Letters*, *30*(10), 1529. https://doi.org/10.1029/2002GL016513

Remya, B., Tsurutani, B. T., Reddy, R. V., Lakhina, G. S., & Hajra, R. (2015). Electromagnetic cyclotron waves in the dayside subsolar outer magnetosphere generated by enhanced solar wind pressure: EMIC wave coherency. *Journal of Geophysical Research: Space Physics*, *120*(9), 7536–7551. https://doi.org/10.1002/2015JA021327

Rodger, C. J., Clilverd, M. A., Green, J. C., & Lam, M. M. (2010). Use of POES SEM-2 observations to examine radiation belt dynamics and energetic electron precipitation into the atmosphere. *Journal of Geophysical Research*, *115*(A4), A04202. https://doi.org/10.1029/2008JA014023

Salice, J. A., Nesse, H., Babu, E. M., Smith-Johnsen, C., & Richardson, I. G. (2023). Exploring the predictability of the high-energy tail of MEE precipitation based on solar wind properties. *Journal of Geophysical Research: Space Physics*, *128*(3), e2022JA031194. https://doi.org/10.1029/2022JA031194

Sandanger, M. I., Ødegaard, L.-K. G., Nesse Tyssøy, H., Stadsnes, J., Søraas, F., Oksavik, K., & Aarsnes, K. (2015). In-flight calibration of NOAA POES proton detectors—Derivation of the MEPED correction factors. *Journal of Geophysical Research: Space Physics*, *120*(11), 9578–9593. https://doi.org/10.1002/2015JA021388

Sergeev, V., Nishimura, Y., Kubyshkina, M., Angelopoulos, V., Nakamura, R., & Singer, H. (2012). Magnetospheric location of the equatorward prebreakup arc. *Journal of Geophysical Research*, *117*(A1), A01212. https://doi.org/10.1029/2011JA017154

Sergeev, V. A., Sazhina, E. M., Tsyganenko, N. A., Lundblad, J. A., & Soraas, F. (1983). Pitch-angle scattering of energetic protons in the magnetotail current sheet as the dominant source of their isotropic precipitation into the nightside ionosphere. *Planetary and Space Science*, *31*(10), 1147–1155. https://doi.org/10.1016/0032-0633(83)90103-4

Sergeev, V. A., & Tsyganenko, N. A. (1982). Energetic particle losses and trapping boundaries as deduced from calculations with a realistic magnetic field model. *Planetary and Space Science*, *30*(10), 999–1006. https://doi.org/10.1016/0032-0633(82)90149-0

Shekhar, S., Millan, R., & Smith, D. (2017). A statistical study of the spatial extent of relativistic electron precipitation with polar orbiting environmental satellites. *Journal of Geophysical Research: Space Physics*, *122*(11), 11274–11284. https://doi.org/10.1002/2017JA024716

Shumko, M., Gallardo-Lacourt, B., Halford, A. J., Liang, J., Blum, L. W., Donovan, E., et al. (2021). A strong correlation between relativistic electron microbursts and patchy aurora. *Geophysical Research Letters*, *48*(18), e2021GL094696. https://doi.org/10.1029/2021GL094696

Smith, D. M., Casavant, E. P., Comess, M. D., Liang, X., Bowers, G. S., Selesnick, R. S., et al. (2016). The causes of the hardest electron precipitation events seen with SAMPEX. *Journal of Geophysical Research: Space Physics*, *121*(9), 8600–8613. https://doi.org/10.1002/2016JA022346

Song, P., DeZeeuw, D. L., Gombosi, T. I., Groth, C. P. T., & Powell, K. G. (1999). A numerical study of solar wind—Magnetosphere interaction for northward interplanetary magnetic field. *Journal of Geophysical Research*, *104*(A12), 28361–28378. https://doi.org/10.1029/1999JA900378

Summers, D., Ni, B., & Meredith, N. P. (2007). Timescales for radiation belt electron acceleration and loss due to resonant wave-particle interactions: 2. Evaluation for VLF chorus, ELF hiss, and electromagnetic ion cyclotron waves. *Journal of Geophysical Research*, *112*(A4), A04207. https://doi.org/10.1029/2006JA011993

Thorne, R. M., Smith, E. J., Burton, R. K., & Holzer, R. E. (1973). Plasmaspheric hiss. *Journal of Geophysical Research*, *78*(10), 1581–1596. https://doi.org/10.1029/ja078i010p01581

Tsurutani, B. T., Falkowski, B. J., Pickett, J. S., Santolik, O., & Lakhina, G. S. (2015). Plasmaspheric hiss properties: Observations from polar. *Journal of Geophysical Research: Space Physics*, *120*(1), 414–431. https://doi.org/10.1002/2014JA020518

Tsurutani, B. T., Falkowski, B. J., Verkhoglyadova, O. P., Pickett, J. S., Santolik, O., & Lakhina, G. S. (2011). Quasi-coherent chorus properties: 1. Implications for wave-particle interactions. *Journal of Geophysical Research*, *116*(A9), A09210. https://doi.org/10.1029/2010JA016237

Tsurutani, B. T., Hajra, R., Tanimori, T., Takada, A., Remya, B., Mannucci, A. J., et al. (2016). Heliospheric plasma sheet (HPS) impingement onto the magnetosphere as a cause of relativistic electron dropouts (REDs) via coherent EMIC wave scattering with possible consequences for climate change mechanisms. *Journal of Geophysical Research: Space Physics*, *121*(10), 10–130. https://doi.org/10.1002/2016JA022499

Tsurutani, B. T., & Lakhina, G. S. (1997). Some basic concepts of wave particle interactions in collisionless plasmas. *Reviews of Geophysics*, *35*(4), 491–501. https://doi.org/10.1029/97rg02200

Tsurutani, B. T., Lakhina, G. S., & Verkhoglyadova, O. P. (2013). Energetic electron (>10 keV) microburst precipitation, 5-15 s X-ray pulsations, chorus and wave-particle interactions: A review. *Journal of Geophysical Research: Space Physics*, *118*(5), 1–17. https://doi.org/10.1002/jgra.50264

Tsyganenko, N. A., & Sitnov, M. I. (2007). Magnetospheric configurations from a high-resolution data-based magnetic field model. *Journal of Geophysical Research*, *112*(A6), A06225. https://doi.org/10.1029/2007JA012260

Tyssøy, H. N., Partamies, N., Babu, E. M., Smith-Johnsen, C., & Salice, J. (2021). The predictive capabilities of the auroral electrojet index for medium energy electron precipitation. *Frontiers in Astronomy and Space Sciences*, *8*, 714146. https://doi.org/10.3389/fspas.2021.714146

West, H. I., Jr., Buck, R. M., & Walton, J. R. (1972). Shadowing of electron azimuthal-drift motions near the noon magnetopause. *Nature Physical Science*, *240*(97), 6–7. https://doi.org/10.1038/physci240006a0

Wing, S., Johnson, J. R., Turner, D. L., Ukhorskiy, A. Y., & Boyd, A. J. (2022). Untangling the solar wind and magnetospheric drivers of the radiation belt electrons. *Journal of Geophysical Research: Space Physics*, *127*(4), e2021JA030246. https://doi.org/10.1029/2021JA030246

Yahnin, A. G., Yahnina, T. A., Semenova, N. V., Gvozdevsky, B. B., & Pashin, A. B. (2016). Relativistic electron precipitation as seen by NOAA POES. *Journal of Geophysical Research: Space Physics*, *121*(9), 8286–8299. https://doi.org/10.1002/2016JA022765

Yando, K., Millan, R. M., Green, J. C., & Evans, D. S. (2011). A Monte Carlo simulation of the NOAA POES medium energy proton and electron detector instrument. *Journal of Geophysical Research*, *116*(A10), A10231. https://doi.org/10.1029/2011JA016671

Zhang, Y. C., Shen, C., Marchaudon, A., Rong, Z. J., Lavraud, B., Fazakerley, A., et al. (2016). First in situ evidence of electron pitch angle scattering due to magnetic field line curvature in the Ion diffusion region. *Journal of Geophysical Research: Space Physics*, *121*(5), 4103–4110. https://doi.org/10.1002/2016JA022409

Zhou, X. Y., & Tsurutani, B. T. (2001). Interplanetary shock triggering of nightside geomagnetic activity: Substorms, pseudobreakups and quiescent events. *Journal of Geophysical Research*, *106*(A9), 18957–18967. https://doi.org/10.1029/2000ja003028